Laboratory of Computational Physics

by Luca Cassia

Dipartimento di Fisica, Università di Milano-Bicocca
I-20126 Milano, Italy

Email: l.cassia@campus.unimib.it

Table of contents

1 Ising Model 2*d* 1

1.1 Thermalization 2
1.2 Estimators and Autocorrelation Times 4
1.3 Binning Analysis 6
1.4 Observables 9
1.5 Probability Distribution Functions 12
1.6 Spatial Correlations 12
1.7 Finite size scaling 13

1 Ising Model 2*d*

In this section we study the statistical properties of a $2d$ Ising Model. We consider a system of $L \times L$ spins situated on the points of a regular square lattice with periodic boundary conditions in both directions. Each spin interacts with its nearest neighbours inside the lattice, with an Hamiltonian:

$$H = \sum_{\langle i,j \rangle} \sigma_i \sigma_j \tag{1}$$

where the sum is taken only over the set of unordered pairs $\langle i, j \rangle$ such that σ_i and σ_j are nearest neighbours.

In order to obtain expectation values for physical quantities of the system we should be able to sum over the space of all the spin configurations, or at least to sample configurations from this space with probability:

$$P(\{\sigma\}) \sim \mathrm{e}^{-\beta H(\{\sigma\})} \tag{2}$$

which reproduces the integration measure of the functional integral. The obvious choice for numerical simulations is the second one, which we implement through Monte Carlo algorithms. In particular we focus on the Metropolis-Hastings (MH) and the Swendsen-Wang (SW) algorithms.

1.1 Thermalization

Since we do not know where to start in our Markov process, we first initialize the system in a disordered configuration (hot start) and then evolve for a certain Markov time until the system reaches equilibrium. This process is usually called *thermalization*.

After a few run we decided to opt for a cold start approach (i.e., all the spins are initially aligned). The reason for this choice is that in 2-dimensional finite-size systems with periodic boundary conditions the non trivial topology of the lattice allows the existence of stable configurations of the type depicted in (Fig.1), that often arise when the system is rapidly cooled from a disordered configuration. Those configurations would invalidate the mixing process and the sampling of relevant configurations at low temperatures. Therefore, by using a cold start, we exclude this possibility.

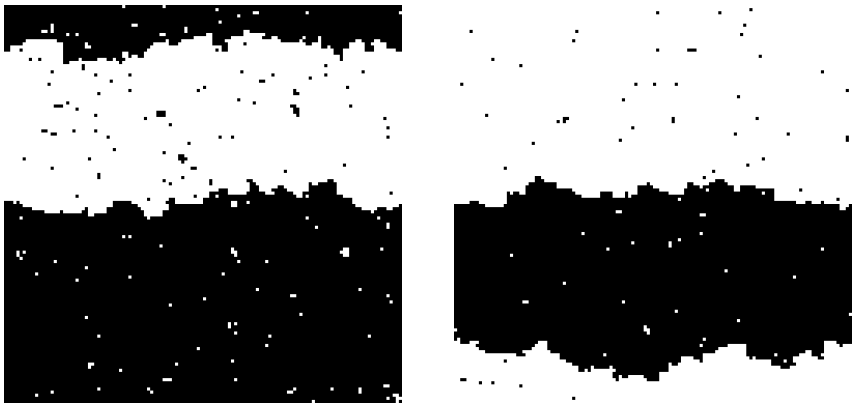

Figure 1. Illustration of two topologically non-trivial configurations on a lattice 128×128.

We expect the MH algorithm to be slower to thermalize because of the local update it employes as opposed to the cluster update of the SW algorithm.

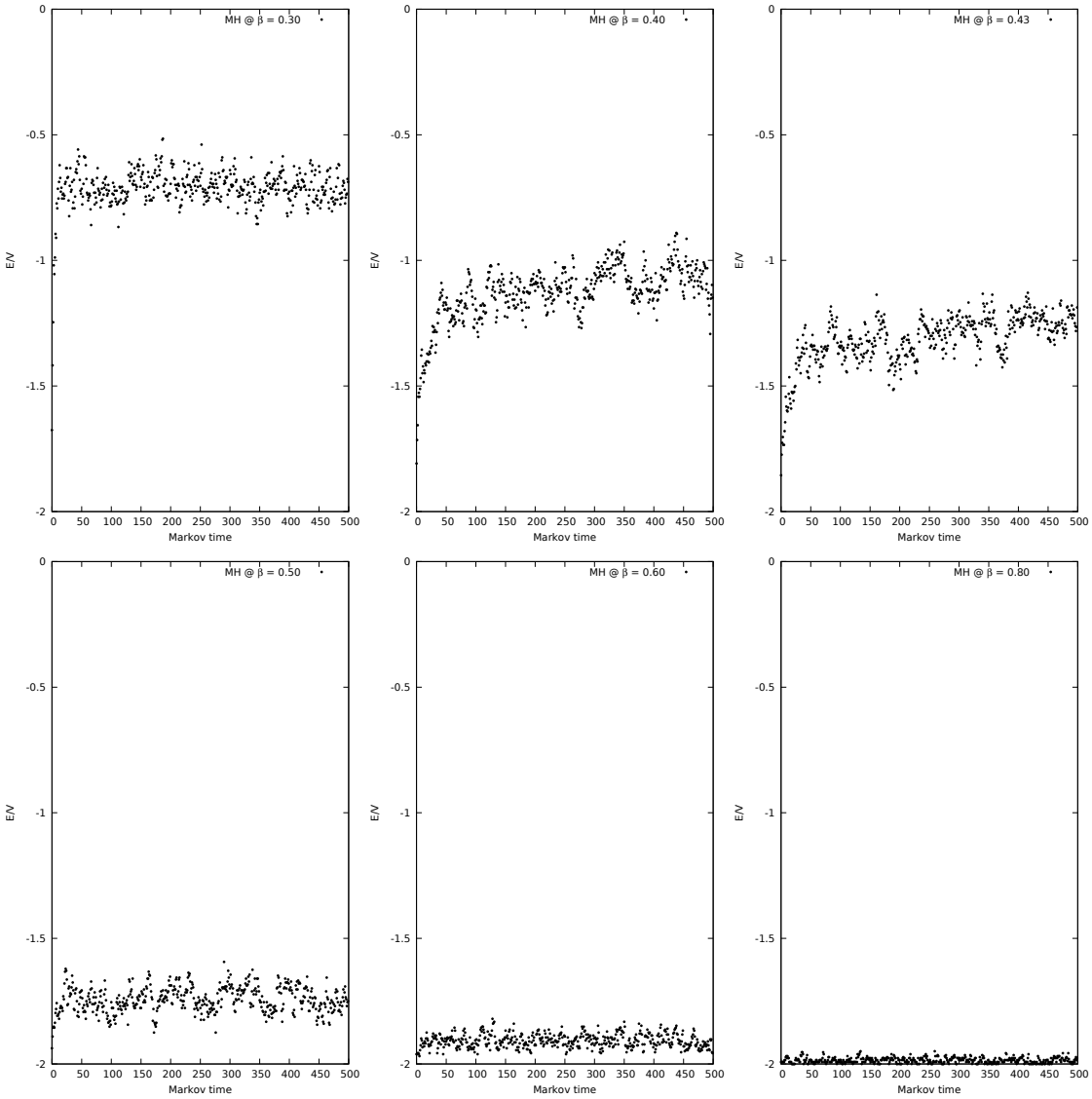

Figure 2. Plot of the energy density for the MH markov process at different values of β ($L = 32$).

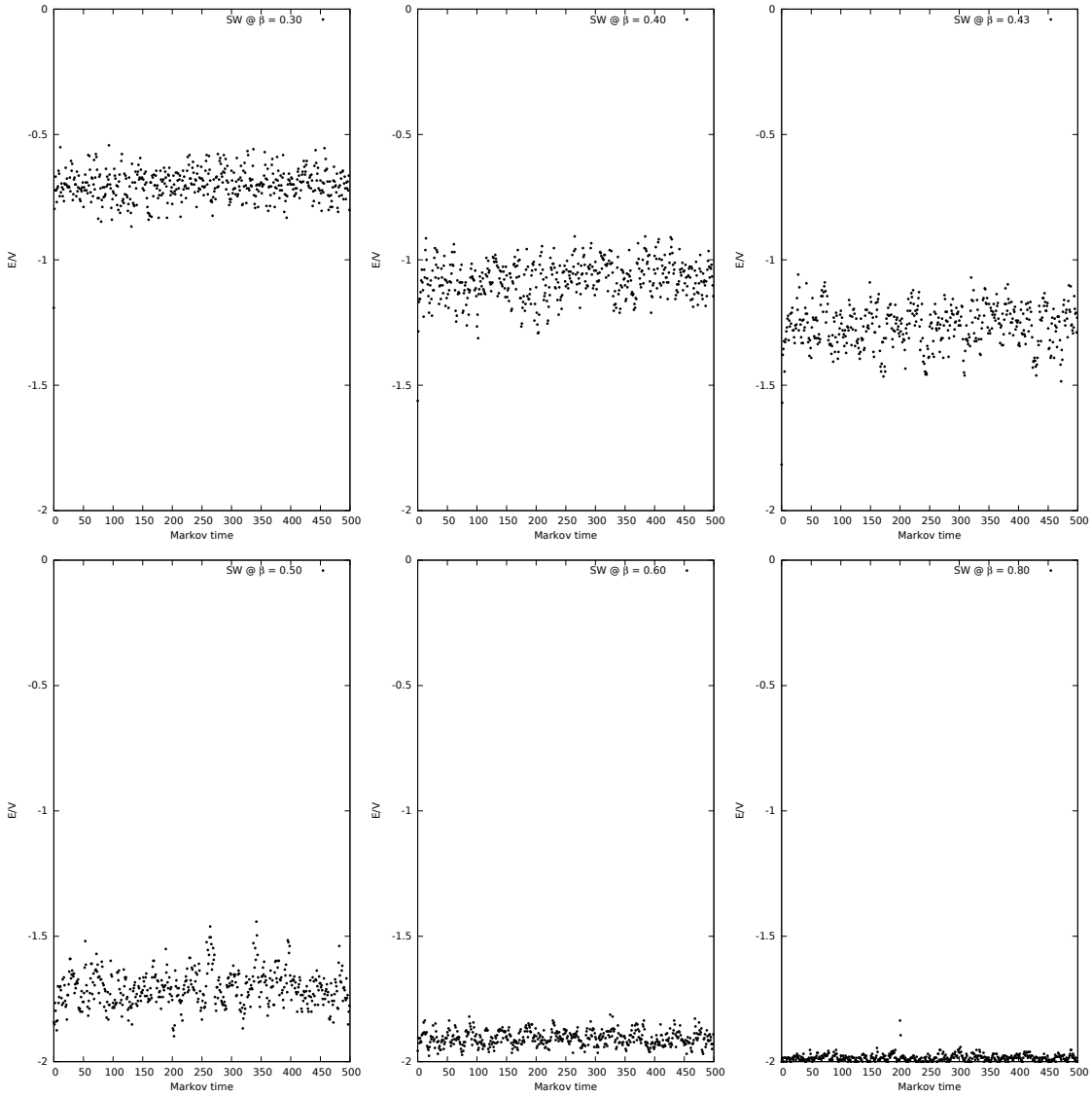

Figure 3. Plot of the energy density for the SW markov process at different values of β ($L = 32$).

The MH algorithm reaches thermalization very rapidly for inverse temperatures β far from the critical value β_c, while for values of β near the phase transition it becomes much slower (Fig.2). This effect is called *critical slowing down* and it tells us that, when using local update algorithms, successive steps in the Markov chain are strongly correlated and therefore only approximately every L^2 sweeps through the lattice, a statistically independent measurement can be taken. Close to a critical point, in fact, the autocorrelation time (in the infinite-volume limit) typically scales as:

$$\tau_{\mathcal{O},\exp} \propto \xi^z \tag{3}$$

where $z \geq 0$ is the so-called dynamical critical exponent. The spatial correlation length ξ would diverge at the critical point, but in a finite system it is limited by the size L of the system and the scaling law (3) becomes:

$$\tau_{\mathcal{O},\exp} \propto L^z \tag{4}$$

where $z \approx 2$ for local dynamics (MH).

We also remark that for smaller values of β, the energy of the system can have larger fluctuations around its average and therfore thermal equilibrium is reached faster.

On the other hand the SW algorithm mixes very fast even at the phase transition (Fig.3) being a multicluster update algorithm (Fig.3).

For the rest of the simulations we used a thermalization time $t_{\text{thermalization}} = 1000$ both for MH and for SW.

1.2 Estimators and Autocorrelation Times

We now study the correlations present between consecutive configurations sampled by the two algorithms in order to obtain the characteristic time after which we can consider two configurations to be statistically independent. This is called *integrated autocorrelation time* and is computed in the following way:

$$\tau_{\mathcal{O},\text{int}} = \frac{1}{2} + \sum_{k=1}^{k_{\max}} R(k) \tag{5}$$

where $\mathcal{O}$ is the physical observable for which we compute autocorrelation and $R(k)$ is defined as:

$$R(k) = \frac{1}{(n-k)\,\sigma^2} \sum_{t=1}^{n-k} (\mathcal{O}_t - \mu)(\mathcal{O}_{t+k} - \mu) \tag{6}$$

here n is the total number of samples of $\mathcal{O}_t$ and μ, σ^2 are the mean and variance of the process.

For large time separations k, $R(k)$ decays exponentially:

$$R(k) \xrightarrow{k\to\infty} r\mathrm{e}^{-k/\tau_{\mathcal{O},\mathrm{exp}}} \tag{7}$$

which defines the exponential autocorrelation time $\tau_{\mathcal{O},\mathrm{exp}}$.

We immediately see from (Fig.4) that the MH process is strongly correlated in time particularly near the phase transition:

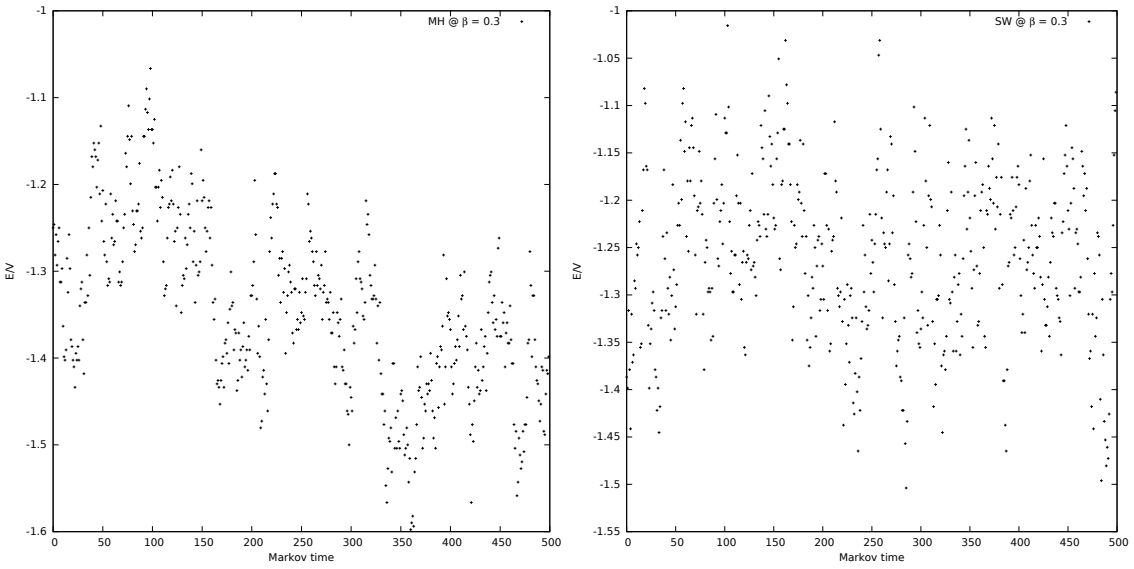

Figure 4. Comparison of the energy for the two algorithms at $\beta = 0.43$. (Left) MH (Right) SW.

We now compute the autocorrelation time τ_{int} for the observable e using formula (5).

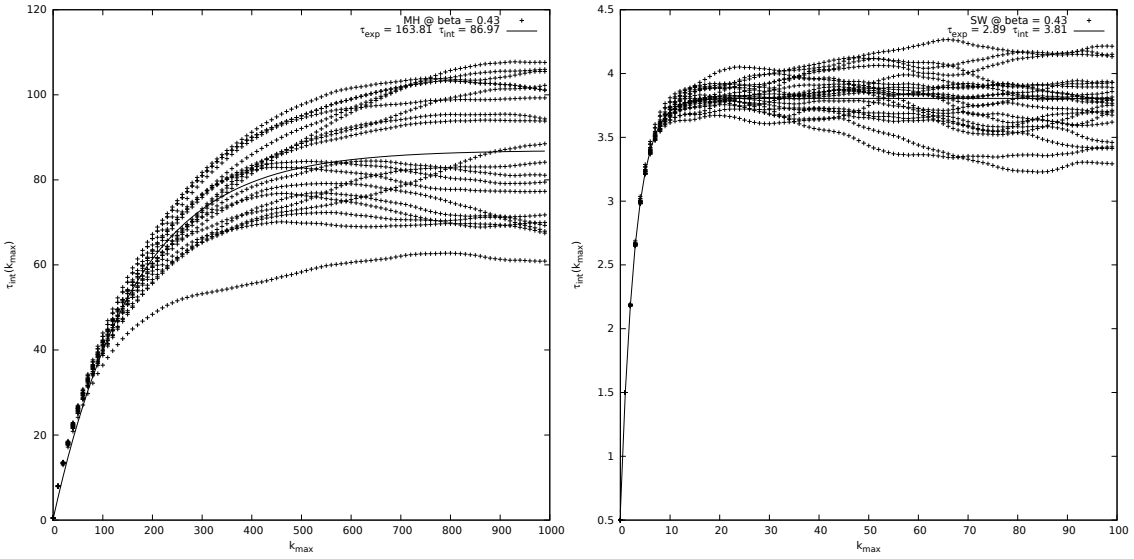

Figure 5. Plot of the integrated autocorrelation time near the phase transition. (Left) MH (Right) SW.

The data is fitted using the function:

$$\tau_{\rm int}(k_{\rm max}) = \tau_{\rm int}\left[1 - \frac{2\,\tau_{\rm exp}}{2\,\tau_{\rm exp}+1}\,{\rm e}^{-k_{\rm max}/\tau_{\rm exp}}\right] \tag{8}$$

As we can see, near the phase transition the autocorrelation time for the MH process becomes very large compared to the autocorrelation time of the SW process. In fact due to the critical slowing down of the MH algorithm, we have $\tau_{\rm int}^{\rm MH} \sim 100$ compared to an autocorrelation time $\tau_{\rm int}^{\rm SW} \sim 5$ for SW (Fig.6).

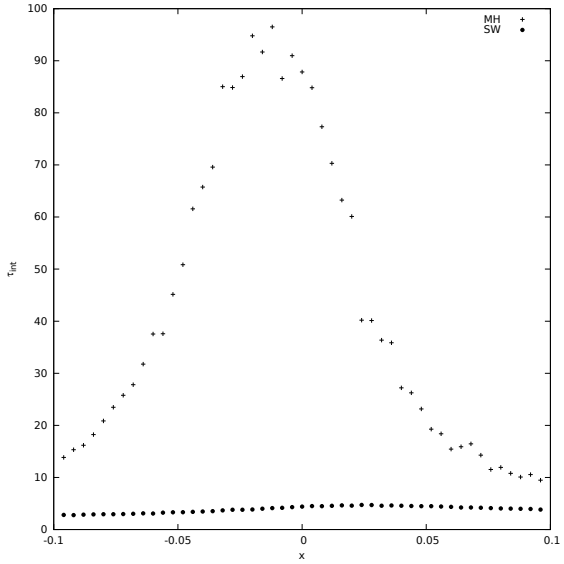

Figure 6. Plot of the integrated autocorrelation time as a function of $x = \frac{\beta - \beta_c}{\beta_c}$.

We remark that the peak is slightly off centered because of the finite size of the lattice ($L = 32$).

1.3 Binning Analysis

In order to have a statistical ensamble of uncorrelated data we need to address the issue of autocorrelation in the Markov process. An easy and efficient way to do so is to split the data in non-overlapping blocks of the same size and then average over each block to obtain (almost)uncorrelated data for the observable $\mathcal{O}$ of interest. The blocks are also called *bins* and this method is called binning.

Consider an ensamble of $N = N_B \cdot k$ samples divided in N_B blocks of size k. For each block n we take the average of the observables $\mathcal{O}_i$ it contains and then obtain a block-observable $\mathcal{O}_{B,n}$:

$$\mathcal{O}_{B,n} = \frac{1}{k}\sum_{i=0}^{k-1} \mathcal{O}_{nk+i} \qquad n = 0, \ldots, N_B - 1 \tag{9}$$

From a simple calculation we obtain that the error estimate on the mean value is:

$$\epsilon^2_{\bar{\mathcal{O}}} \equiv \sigma^2_{\bar{\mathcal{O}}} = \frac{\sigma_B^2}{N_B} = 2\,\tau_{\mathcal{O},\rm int}\,\frac{\sigma^2_{\mathcal{O}_i}}{N} \tag{10}$$

hence:

$$2\,\tau_{\mathcal{O},\rm int} = k\,\sigma_B^2 / \sigma^2_{\mathcal{O}_i} \tag{11}$$

We study the dependence of the variance σ_B^2 on the block size k. The observable we consider is the energy density e.

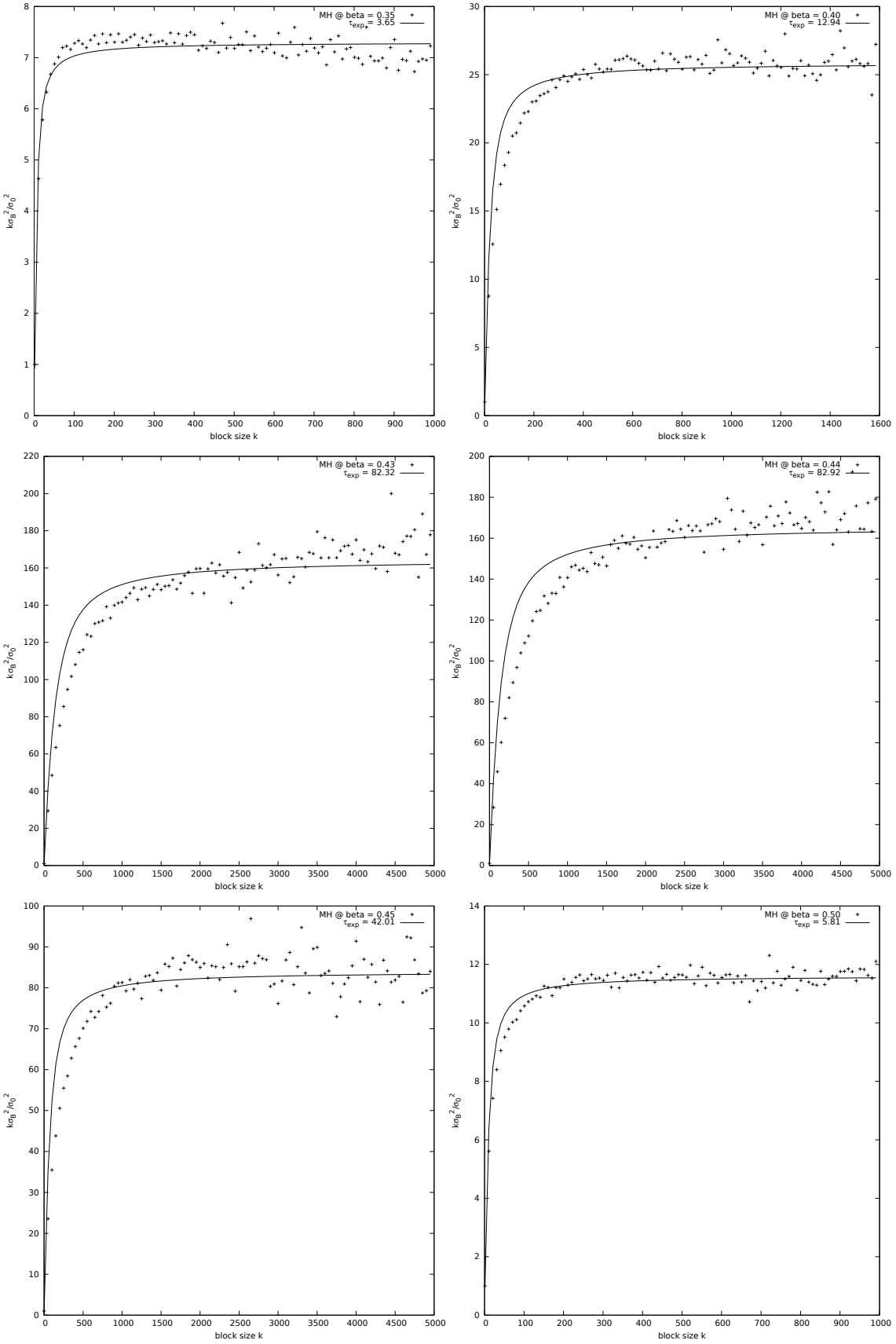

Figure 7. Binning analysis for the MH algorithm at various values of β.

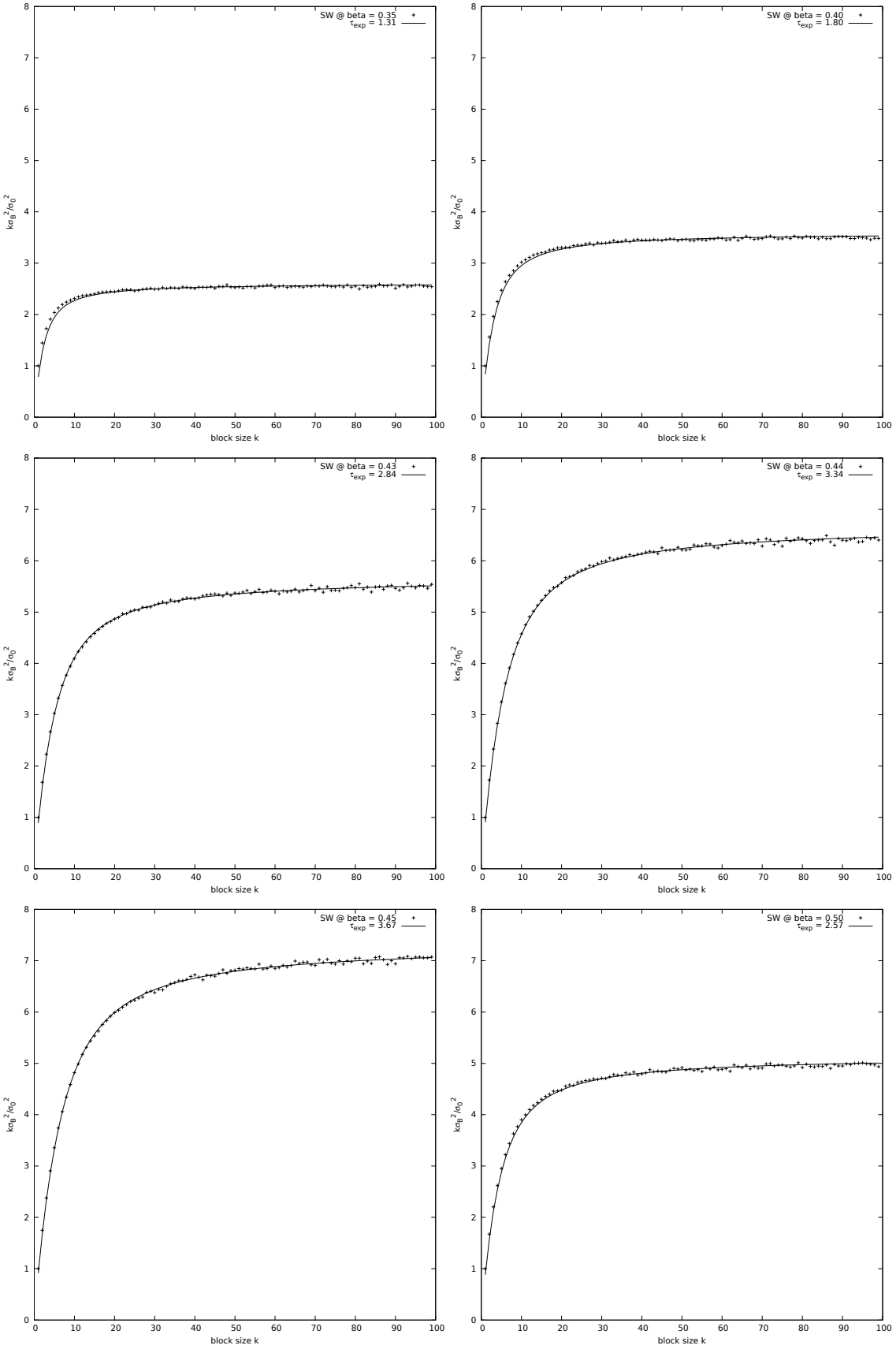

Figure 8. Binning analysis for the SW algorithm at various values of β.

Where we fitted the data using the formula:

$$k\,\sigma_B^2 \approx 2\,\tau_{\exp}\left(1-\frac{\tau_{\exp}}{k}\left(1-\mathrm{e}^{-k/\tau_{\exp}}\right)\right) \tag{12}$$

The lowest value of k for which we can consider the binned data to be uncorrelated is obtained by looking at the point for which the signal for $k\,\sigma_B^2\,/\,\sigma_{\mathcal{O}_i}^2$ stabilizes and its first derivarive tends to zero. We call this point $k^*(\beta)$. Since $\tau_{\exp}$ has a local maximum at the critical point, we take $k^*(\beta_c)$ as the block size for the following simulations.

With the block sizes set to:

$$\begin{aligned} k^*_{\mathrm{MH}} &= 1000 \\ k^*_{\mathrm{SW}} &= 50 \end{aligned}$$

we are now able to sample data without worrying about autocorrelation in the signal.

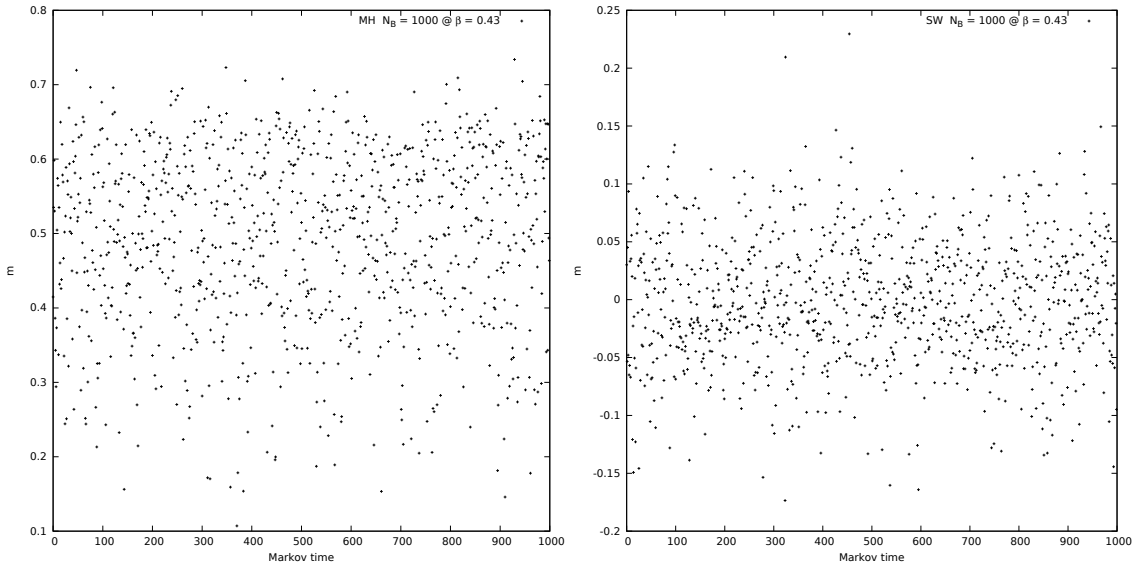

Figure 9. Sampled data after the binning. MH on the left and SW on the right. As we can see the signal loses almost all of its autocorrelation after the binning.

1.4 Observables

The main observables of interest for this system are the energy density e and the magnetization m:

$$e = E/V, \qquad E = \langle \mathcal{H} \rangle, \qquad V = L^d \tag{13}$$

$$m = M/V = \langle |\mu| \rangle, \qquad \mu = \sum_i \sigma_i / V \tag{14}$$

Thanks to the analytical solution of the $2d$ Ising model, first obtained by Onsager, we are able to compare the estimators obtained by numerical simulations with their exact values obtained analytically.

The samples are collected employing the binning procedure of the previous section.

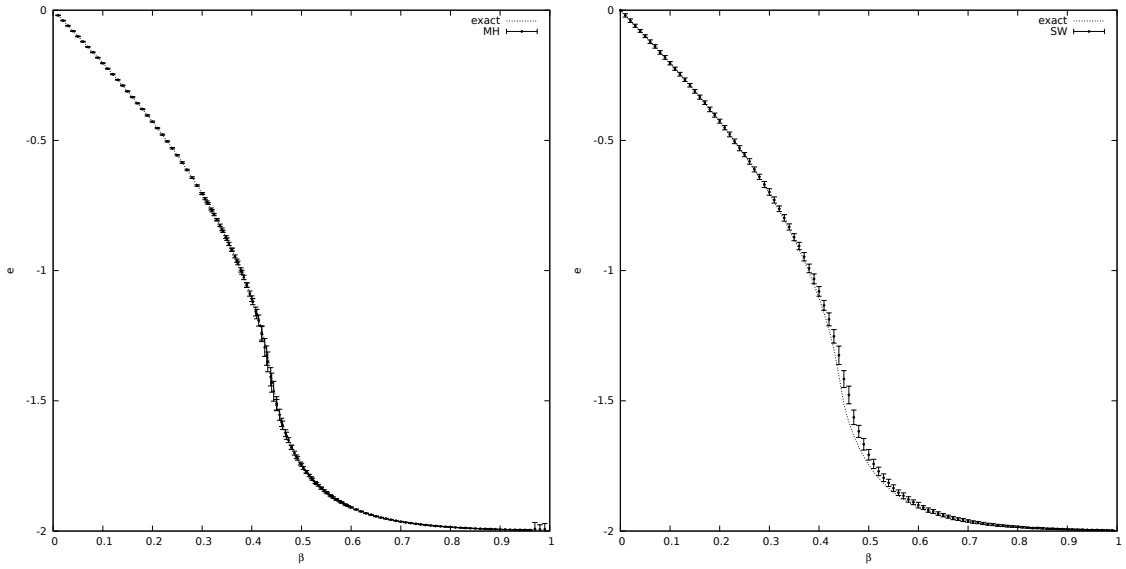

Figure 10. Energy density as a function of β. MH on the left and SW on the right. The energy and the errors are computed from a sample of 100 blocks of binned data on a 32×32 lattice.

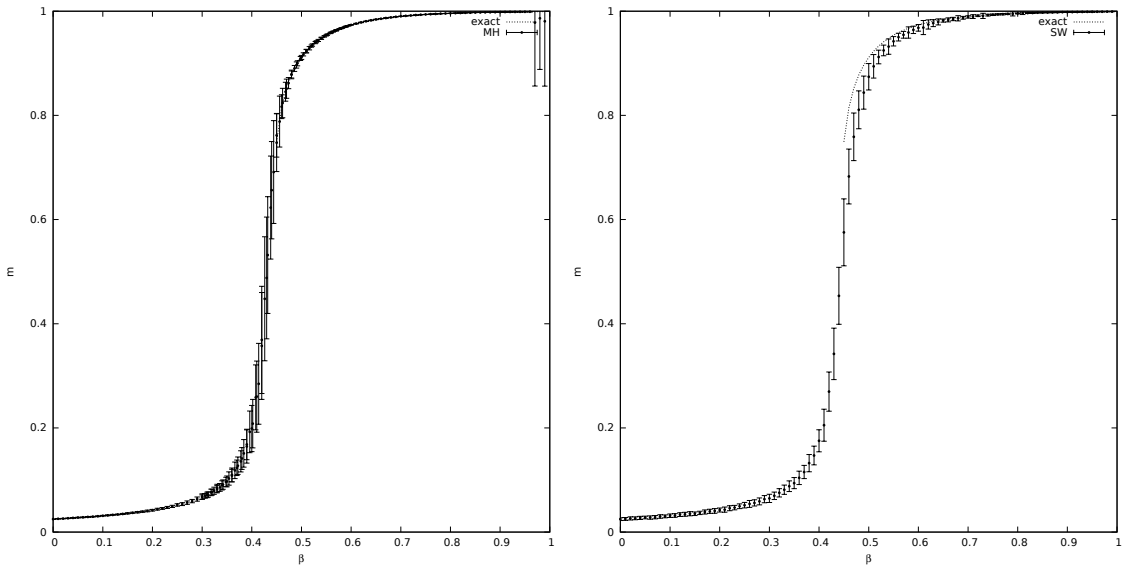

Figure 11. Magnetization as a function of β. MH on the left and SW on the right.

We find that the simulation data are remarkably close to the exact solution both for the energy density and for the magnetization. The only departure from Onsager's solution is in the paramagnetic phase of the magnetization plot: there we observe that the exact solution goes abruptly to zero before the critical point, while the numerical data seems to interpolate a smooth function. This is imputable to the finite size of the lattice used for the simulation. It is indeed a well known fact that discontinuities and divergences only appear in the thermodinamic limit of infinite size, which is precisely the premise of Onsager's solution.

In section (1.7) we will see that as we scale the size of the lattice the numerical solution will approach more and more the exact one.

We also plot the variance of e and m which are respectively proportional to the heat capacity c and the magnetic susceptibility χ:

$$c = V\left(\left\langle\left(\frac{\mathcal{H}}{V}\right)^2\right\rangle - \left\langle\left(\frac{\mathcal{H}}{V}\right)\right\rangle^2\right) \tag{15}$$

$$\chi = V\left(\langle\mu^2\rangle - \langle|\mu|\rangle^2\right) \tag{16}$$

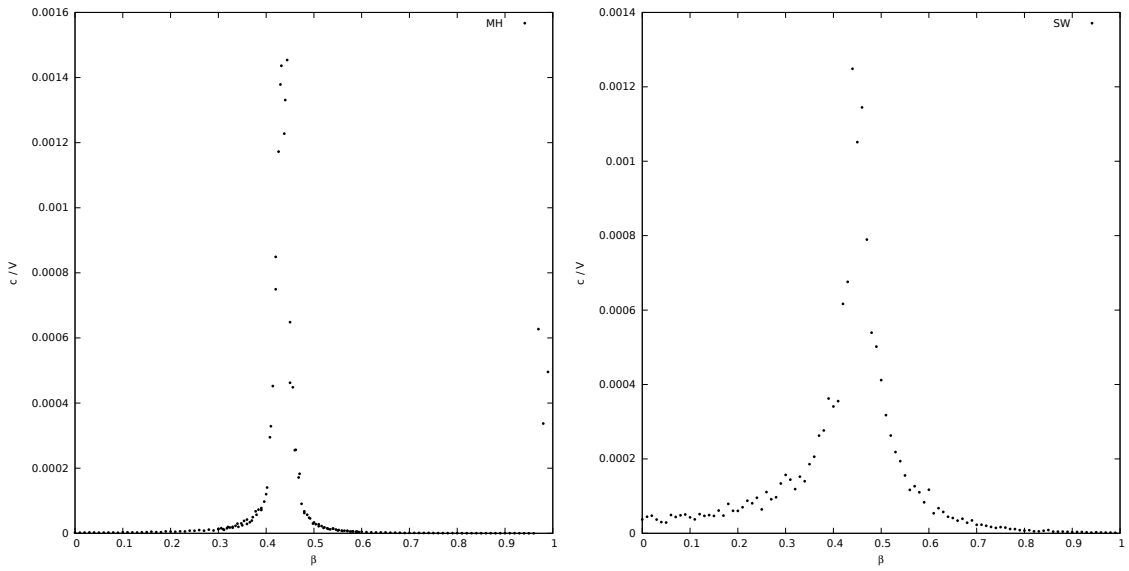

Figure 12. Heat capacity as a function of β. MH on the left and SW on the right.

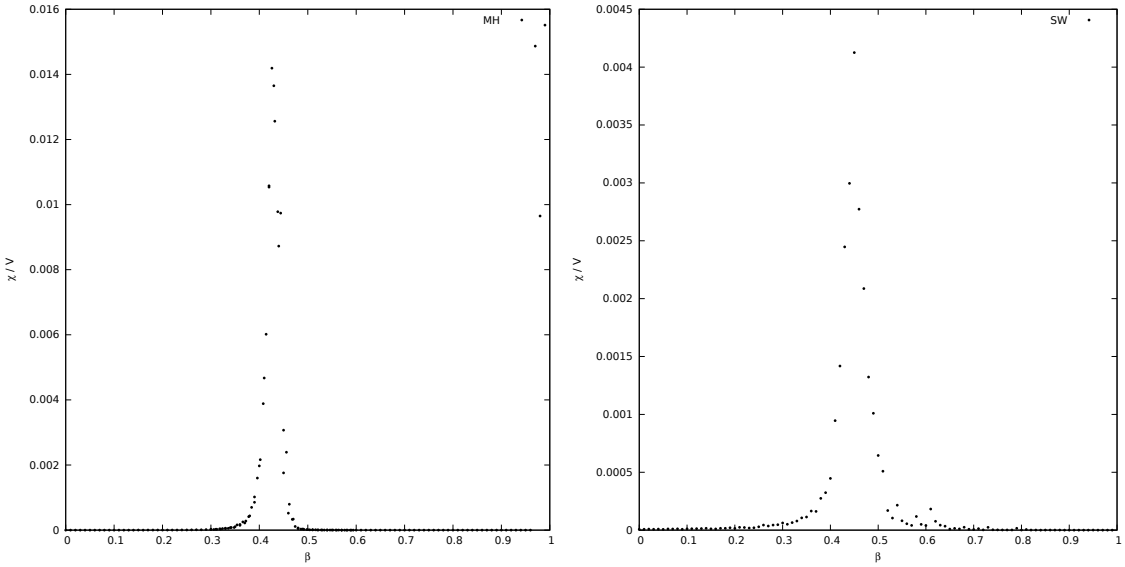

Figure 13. Magnetic susceptibility as a function of β. MH on the left and SW on the right.

1.5 Probability Distribution Functions

We study the probability distribution of the magnetization:

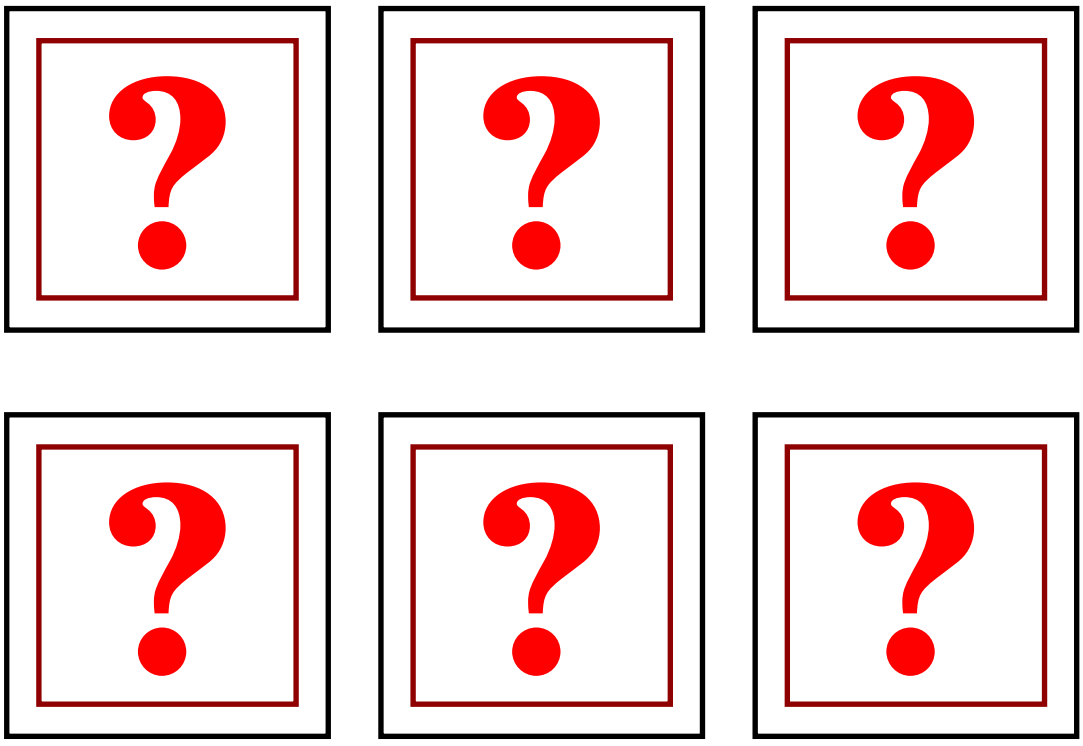

Figure 14. Probability distribution function of m for various values of β ($L = 32$).

We see from (Fig.14) that the width of the distribution gets larger as β approaches the critical value β_c. This is in fact what we expect, knowing that the susceptibility diverges at a second order phase transition.

1.6 Spatial Correlations

Correlation functions are defined as:

$$G(\vec{x}_i - \vec{x}_j) = \langle \sigma_i \sigma_j \rangle \quad \sim \quad \exp(-|\vec{x}_i - \vec{x}_j| / \xi) \quad \text{for large} \quad |\vec{x}_i - \vec{x}_j| \tag{17}$$

where ξ is the correlation length of the system:

$$\xi = -\lim_{|\vec{x}| \to \infty} (|\vec{x}| / \ln G(\vec{x})) \tag{18}$$

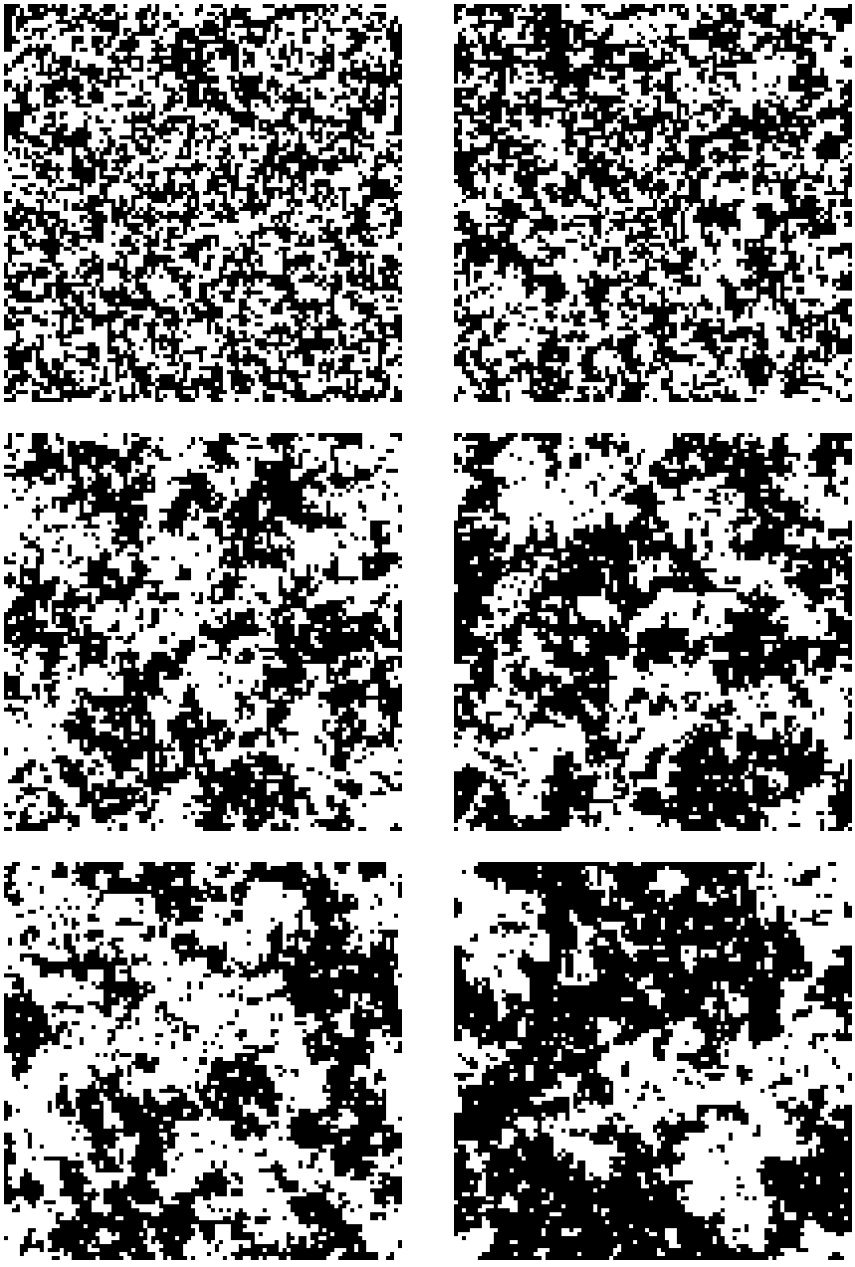

Figure 15. Ilustration of the growth of spatial correlations when criticality is approached on a lattice 100×100 : $\beta = 0.22, 0.31, 0.37, 0.39, 0.42, 0.43$

1.7 Finite size scaling